

# Diamond-like carbon for magnetic storage disks

Andrea Carlo Ferrari\*

*Department of Engineering, University of Cambridge, Cambridge, CB2 1PZ, UK*

## Abstract

Diamond-like carbon films form a critical protective layer on magnetic hard disks and their reading heads. The ultimate limit to storage density is the super-paramagnetic limit, where the thermal energy is able to overcome the coercive energy of the magnetic bit. Perpendicular recording should allow storage densities up to  $\sim 1$  Tbit/inch<sup>2</sup>. This requires the read head to approach closer to the magnetic layer and ever-thinner layers of carbon 1–2 nm thick. A critical review of the properties of the main classes of carbon films used for magnetic storage disks is presented. Tetrahedral amorphous carbon can provide the atomic smoothness, continuity and density required for magnetic storage applications down to a few atomic layers thickness. The main approaches to assess the structural and morphological properties of ultra-thin carbon layers are reviewed. Raman spectroscopy, X-ray reflectivity, atomic force microscopy and surface acoustic waves based methods allow a full non-destructive characterization of ultra-thin carbon layers.

© 2003 Elsevier B.V. All rights reserved.

*Keywords:* Magnetic storage disks; X-ray reflectivity; Surface acoustic waves

## 1. Magnetic storage technology

Magnetic storage is the most economic form of non-volatile storage for many applications [1–14]. Its great advantage is that the storage density is increasing at a very rapid rate [1–5] (Fig. 1). Recently, with the introduction of giant magneto-resistive heads, storage densities are increasing at 100% per year. This is much faster than the Moore's law rate for silicon devices ( $\sim 50\%$  per year).

Data are stored in a magnetic layer of Co–Cr–Pt alloy thin film [6,7]. A protective layer of diamond-like carbon (DLC) coating is applied over the Co layer, and 1–2 monolayers of a perfluoro-polyether such as ZDOL or Fomblin is used as a molecular lubricant. A read/write head flies above the rotating disk on an aerodynamic bearing. The read/write head consists of many layers of thin films and is also protected by a DLC film, Figs. 2 and 3.

The storage density is increased by reducing the area occupied by each bit of data. The areal density is the product of the tracks per inch and the bits per inch along a track. The ratio of tracks per inch and bits per

inch is called the bit-aspect ratio. Initially this ratio was approximately 20 [5]. The ultimate limit to storage density is the super-paramagnetic limit, where the thermal energy  $kT$  can overcome the coercive energy of the magnetic bit [1–14]. In 1995, this limit was approximately 40 Gbits/inch<sup>2</sup>. The limit was increased to 200 Gbits/inch<sup>2</sup> by reducing the bit-aspect ratio to 4 and by using materials of higher coercivity [2–6]. Recently, Seagate and Fujitsu achieved a storage density of 100 Gbits/inch<sup>2</sup> in laboratory demonstrations [15]. One terabit per square inch may be possible, but using perpendicular recording, where the magnetization is normal to the film surface, in contrast to the standard longitudinal recording, where it is parallel to the surface [8,9].

A smaller bit size requires a smaller magnetic spacing, which is the vertical distance between the read head and the Co storage layer, Fig. 3. The magnetic spacing is slightly greater than the fly height, which is the separation of head and disk. Reducing the fly height requires ever-thinner carbon films. They are presently approximately 4 nm thick and need to reach 1–2 nm in the near future [2,3], as shown in Fig. 4. Indeed, in order to achieve the goal of  $\sim 1$  Tbit/inch<sup>2</sup> the magnetic spacing must be reduced to 6.5 nm, which implies a  $\sim 1$  nm head and disk overcoat [16]. This is only approximately 7 atomic layers thick, and the perform-

\*Tel.: +44-1223-765242; fax: +44-1223-332662.

E-mail address: [acf26@eng.cam.ac.uk](mailto:acf26@eng.cam.ac.uk) (A.C. Ferrari).

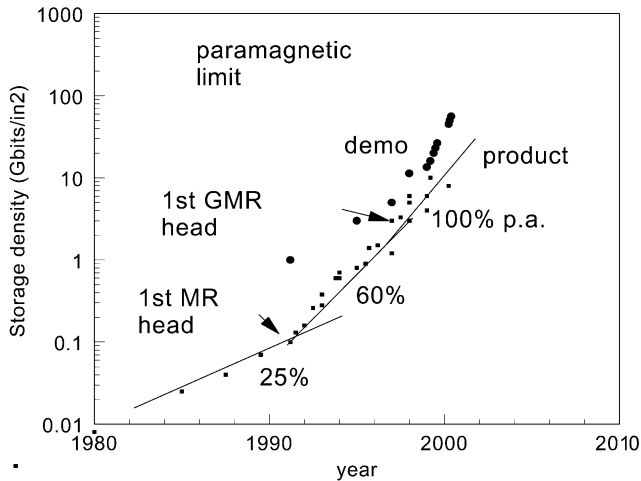


Fig. 1. Growth of storage density with year for magnetic disks. Recent data distinguish between product and lab demonstration [3–5].

ance of the carbon and the processes used to make it change dramatically when we approach 1 nm.

DLC films are used as coatings because they are extremely smooth, continuous and chemically inert, with surface roughness well below 1 nm. For the previous 30 years, DLC has been deposited by sputtering. Now, there is a transition, as the industry moves to new processes such as cathodic arc or plasma deposition needed to make the thinner films. The main role of such ultra-thin films is to provide a corrosion barrier to the recording medium. They must be atomically smooth, dense, continuous and pin-hole free. However, both a-C:N and a-C:H cease to provide protection against corrosion and wear below 3–4 nm thickness since

magnetron sputtering is not able to make continuous and ultra-thin films [17]. Highly  $sp^3$  hydrogen-free DLC, tetrahedral amorphous carbon (ta-C), is now the preferred means of coating read heads, because of its unique combination of desirable properties, such as high hardness and wear resistance and chemical inertness to both acids and alkalis and atomic smoothness. Thus, in this paper we will focus particular attention to the properties and characterization of ultra-thin ta-C films.

DLC films can also be used to coat optical storage media, as discussed in Section 4 [18,19].

## 2. Classification of carbon films

The main properties of the various carbon films are well known, at least for films thicker than 10 nm [20]. Here we present a general classification of carbon films in terms of their bonding and some useful correlations linking mechanical and structural properties of ta-C.

The great versatility of carbon materials arises from the strong dependence of their physical properties on the ratio of  $sp^2$  (graphite-like) to  $sp^3$  (diamond-like) bonds [20]. There are many forms of  $sp^2$  bonded carbons with various degrees of graphitic ordering, ranging from micro-crystalline graphite to glassy carbon. In general, an amorphous carbon can have any mixture of  $sp^3$ ,  $sp^2$  and even  $sp^1$  sites, with the possible presence hydrogen and nitrogen. The compositions of nitrogen-free carbon films are conveniently shown on the ternary phase diagram (Fig. 5a).

We define DLC an amorphous carbon or a-C:H with a significant fraction of  $sp^3$  bonds. a-C:H often has a rather small C–C  $sp^3$  content. ta-C is the form of DLC

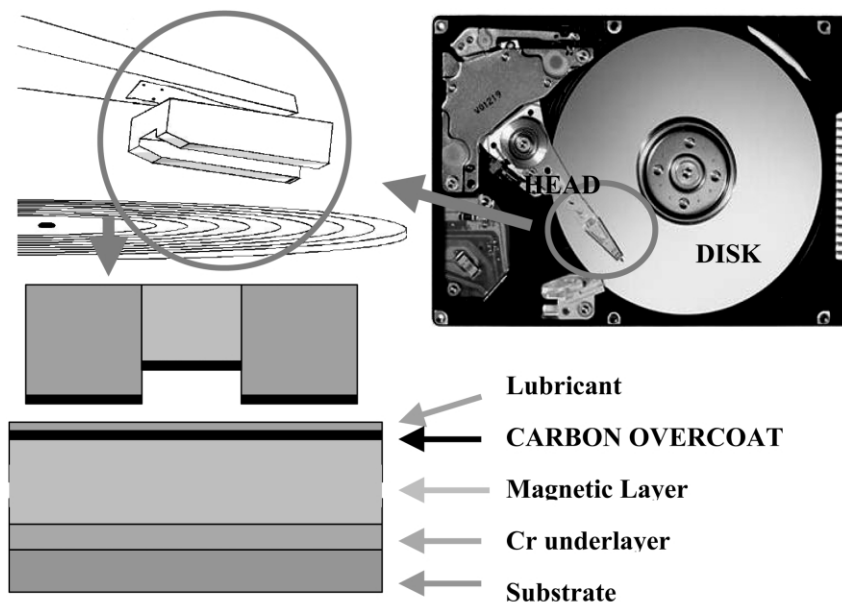


Fig. 2. Hard disk architecture.

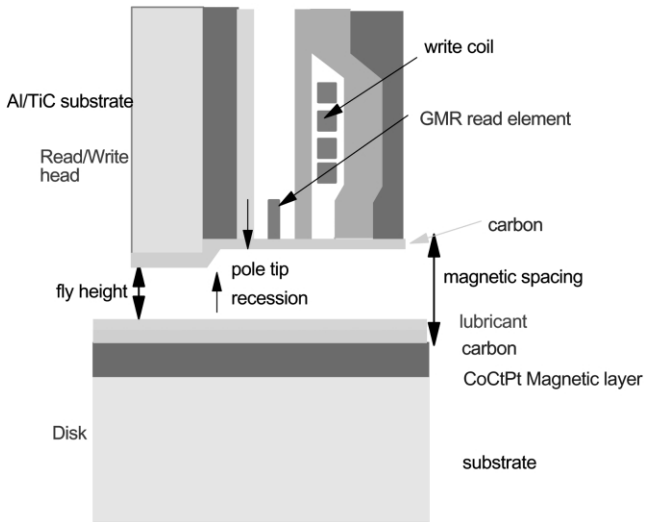


Fig. 3. Cross-section of head/disk interface.

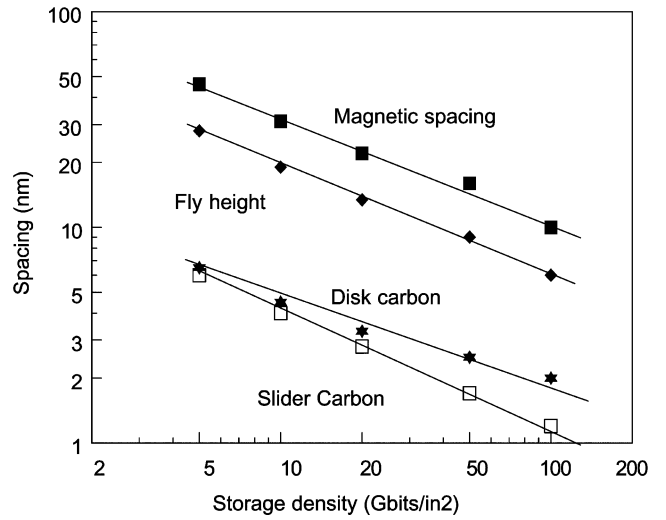


Fig. 4. Variation of carbon thickness on disk and sliders, magnetic spacing and fly height with storage density [3–5].

with the highest  $sp^3$  content (80–90%); its hydrogenated analogue is ta-C:H. The key parameters in such materials are: (1) the  $sp^3$  content; (2) the clustering of the  $sp^2$  phase; (3) the orientation of the  $sp^2$  phase; (4) the

cross-sectional nano-structure; (5) the H content. The  $sp^3$  content alone mainly controls the elastic constants, but films with the same  $sp^3$  and H content but different

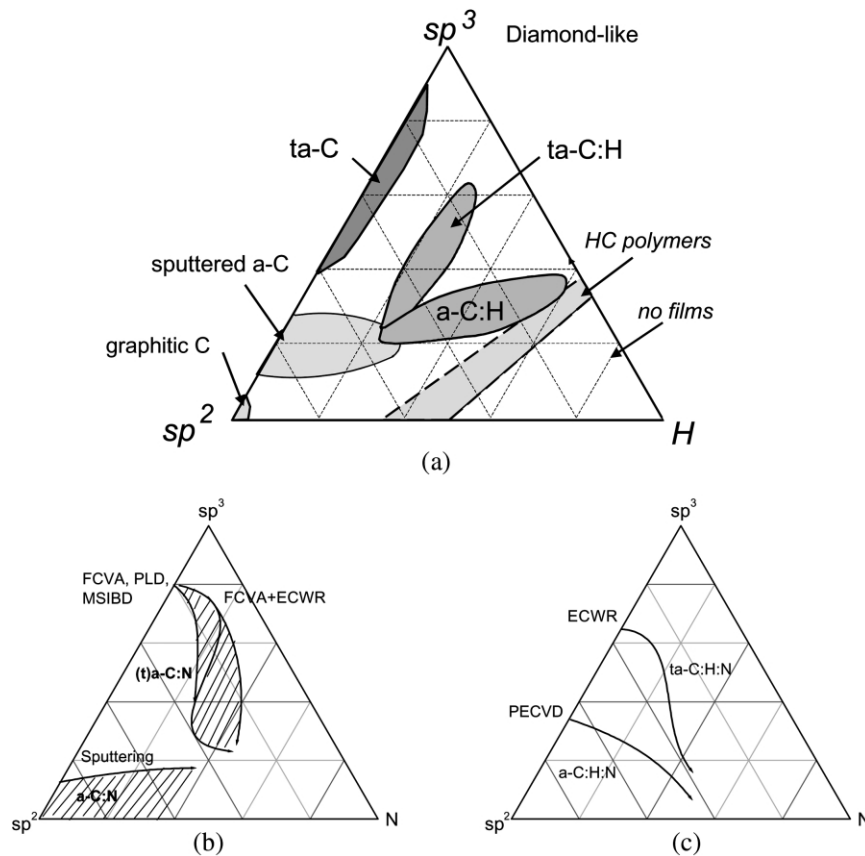


Fig. 5. (a) Ternary phase diagram of amorphous carbons. The three corners correspond to diamond, graphite and hydrocarbons, respectively. (b and c) Ternary phase diagrams of amorphous carbon nitride alloys, without hydrogen (b) or with hydrogen (c), showing  $sp^2$  C,  $sp^3$  C and N.

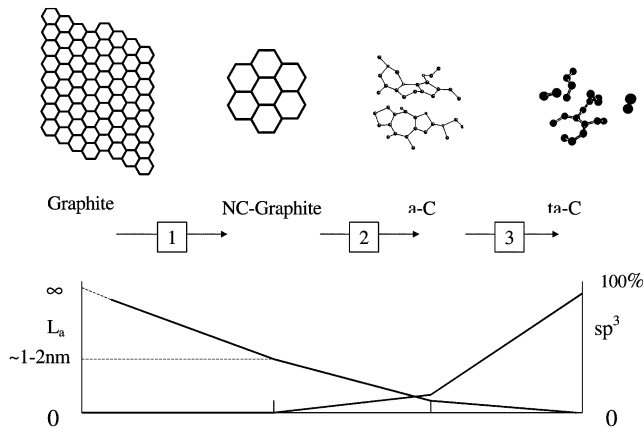


Fig. 6. (a) Variation of the  $sp^2$  configuration along the three amorphisation stages. (b) Schematic comparison of the evolution of the  $sp^2$  cluster size ( $L_a$ ) and  $sp^3$  content. Note that in stages 1–2 to a strong  $sp^2$  cluster size decrease corresponds a relatively small  $sp^3$  increase, whilst the opposite is seen in stage 3.

$sp^2$  clustering,  $sp^2$  orientation or cross-sectional nano-structure can have different optical and electronic properties [20]. As we move from ordered graphite to nano-crystalline graphite (nc-G), to amorphous carbon and finally to  $sp^3$  bonded ta-C, the  $sp^2$  groups become smaller first, then topologically disordered and finally change from ring to chain configurations. The evolution of the  $sp^2$  phase clustering can be represented by the *amorphisation* trajectory of Fig. 6, consisting of three stages from graphite to ta-C: (1) graphite  $\rightarrow$  nc-G; (2) nc-G  $\rightarrow$   $sp^2$  a-C; (3) a-C  $\rightarrow$  ta-C. Note that the  $sp^2$  clustering evolution and the  $sp^3$  content evolution follow two distinct paths (Fig. 6b).

a-C:H for magnetic storage applications is deposited by reactive magnetron sputtering and plasma enhanced chemical vapour deposition. ta-C can be deposited by filtered cathodic vacuum arc (FCVA) or high current arc (HCA). ta-C:H by plasma beam sources and electron cyclotron wave resonance (ECWR) sources [2,3,20].

Fig. 7a plots the relation between density and  $sp^3$  content for ta-C, ta-C:H and a-C:H films. In ta-C many beneficial properties, such as Young's modulus, hardness, density and smoothness correlate directly with the C–C  $sp^3$  fraction. An  $sp^3$  increase is found to correspond linearly to a density increase according to [21]

$$\rho \text{ (g/cm}^3\text{)} = 1.92 + 1.37F \quad (1)$$

where  $F$  is the  $sp^3$  fraction between 0 and 1.

It is also found that the Young's modulus  $E$  scales with the  $sp^3$  fraction as [22]

$$E \text{ (GPa)} = 478.5(F + 0.4)^{1.5} \quad (2)$$

From Eqs. (1) and (2) we can derive a general density

vs. Young's modulus relation for ta-C:

$$\rho \text{ (g/cm}^3\text{)} = 1.37 + [E(\text{GPa})]^{2/3}/44.65. \quad (3)$$

Fig. 7b plots experimental density and  $sp^3$  fraction data and the general correlation resulting from Eq. (3). Fig. 7b demonstrates that Eq. (3) can be very efficiently used for ta-C.

Carbon nitrides are also commonly used in storage applications. We classify the bonding in carbon nitride films into four types, based on the bonding in the corresponding N-free film as defined in Fig. 5a. The changes in the properties of carbon nitride films as N content is increased should be compared with the properties of the corresponding N-free films. Thus, the variation of mechanical and electronic properties when N is added to a  $sp^2$  bonded carbon film differs from when N is added to a high  $sp^3$  film. This is true if H is

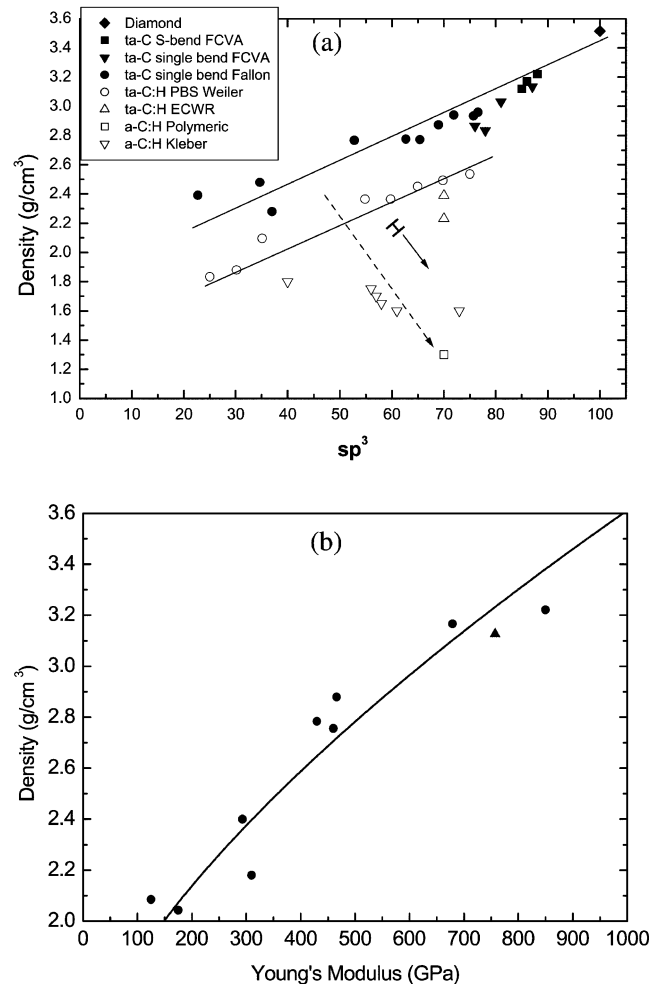


Fig. 7. (a) Density vs.  $sp^3$  fraction for N-free carbon films. Note the similar trends for ta-C and ta-C:H, but the opposite trend for a-C:H of increasing H content [21]. (b) Density vs. Young's modulus for ta-C films. The experimental trend can be well described by Eq. (3), line in the plot.

present or not. We classify carbon nitrides into four types: (a) the mainly  $sp^2$  bonded a-C:N produced by sputtering, (b) the mainly  $sp^3$  bonded ta-C:N produced by cathodic arc, (c) plasma deposited a-C:H:N with moderate  $sp^3$  content and (d) ta-C:H:N prepared by a high plasma density source, with a higher  $sp^3$  content and lower hydrogen content. The corresponding ternary phase diagrams are shown in Fig. 5b and c. Note that, although a general decrease of  $sp^3$  content with N is observed, the trends are different according to the deposition systems [23]. This implies that the  $sp^3$  fraction and the degree of clustering of the  $sp^2$  phase can be different for films of the same N/C ratio [23].

The sputtered a-C:N films deserve particular attention. a-C:N films with a high fraction of  $sp^2$  bonded atoms are produced by DC, RF sputtering or magnetron sputtering and by low energy laser deposition. An unusual aspect of these films is that a-C:N deposited above 200 °C can become nano-structured, with a strong cross-linking between graphitic planes, which gives an increase in mechanical hardness and large elastic recovery [24–26]. This does not require, however, an increase of the  $sp^3$  fraction (Fig. 5b), but can rather be seen as an increase in disorder [25,26]. Thus, N incorporation in this case has an opposite effect to N incorporation in high  $sp^3$  carbons. This beneficial effect is exploited in carbon nitrides used in magnetic storage, since the deposition of the carbon layer on the disk is performed at  $\sim 200$  °C, the process temperature resulting from the magnetic layer deposition.

### 3. Requirements for the carbon overcoat

When first introduced, the role of carbon films was to provide protection against corrosion. Simple a-C was used, deposited by magnetron sputtering. Later, a-C:H was used, produced by the reactive sputtering of graphite in an Ar/hydrogen atmosphere [27], in order to provide also some protection against mechanical wear and damage during head crashes [28–31]. Many groups have emphasized this role of DLC for mechanical protection. However, hardness is not the critical parameter. For example, the optimum hydrogen content of the a-C:H for disk coating was found to be greater than that giving the maximum hardness [6,7,41]. In this case, this optimum composition is thought to arise because the lubricant work prefers a slightly hydrogen-rich surface. On the disk, the carbon should also provide a surface for the perfluoro-polyether lubricant to adhere and move [33,39,40]. This requires the carbon to separate the lubricant and the magnetic substrate. This is critical since Al tends to catalyse the decomposition of the lubricant, and it has been noted that end of life generally corresponds to the onset of lubricant degradation. Thus, the primary role of the carbon film is to be continuous, to give protection against corrosion, and to separate the Co layer and read/write head from the ambient.

More recently, a-C:N is being used instead of a-C:H [31–39]. a-C:N is produced by reactive sputtering of graphite in an Ar/N<sub>2</sub> atmosphere. Nitrogen is usually found to have a beneficial effect on tribological properties [33], even when it decreases the hardness as in ta-C:H:N [36]. Nitrogen appears to increase the toughness of the films, so that a-C:N performs better in micro-scratch tests than a-C:H. This can be explained by the improvement of the mechanical properties, with increase of elastic recovery and toughness observed for high temperature deposited carbon nitride films, as pointed out in Section 2. Another important advantage of a-C:N relates to the lubricant. The carbon separates the lubricant and the substrate. Under stress, the perfluoro-polyether lubricant molecules tend to degrade with the emission of *F*. *F* can abstract H from a-C:H under the local heating to give HF. This then reacts aggressively with the underlying metals. In contrast, heating of a-C:N releases only nitrogen, which will not give rise to HF [42].

However, there is a thickness limit to the beneficial properties of carbon nitride films. It is found that carbon nitride films below 4-nm thickness are not able to protect the magnetic layer sufficiently against corrosion [17,42,43]. For this reason an increasing attention is devoted to ta-C. ta-C allows uniform coverage, corrosion protection, ultra-smooth surfaces and reasonable mechanical properties down to  $\sim 1$ -nm thickness [3–5,10,16,43–48]. The main drawback to the use of ta-C is the filtering of the macroparticles during deposition [49,50]. If this problem is not satisfactorily solved, this may force ta-C to be used only for the head production, whilst it might not be suitable for the disk.

To summarize, the ideal carbon overcoat should be engineered to provide:

1. Corrosion protection, which requires complete coverage and high density
2. Chemical properties, such as lube compatibility, stability and low adsorption
3. Surface topography, such as smoothness, complete coverage and absence of particles
4. Wear resistance, which requires reasonable hardness, low friction and high elasticity
5. Magnetic layer integrity: the deposition process should minimize the 'dead layer' created by the impinging ion particles.

### 4. Optical storage technology

Optical storage is the preferred technology when high-density storage on removable and exchangeable media is required. The advantages are its low cost, media exchangeability (standardization) and robustness. Over the past 20 years, the storage capacity in optical recording has been raised by increasing the numerical aperture of the focussing optics and decreasing the laser wavelength (Fig. 8a.) The new generation of optical storage

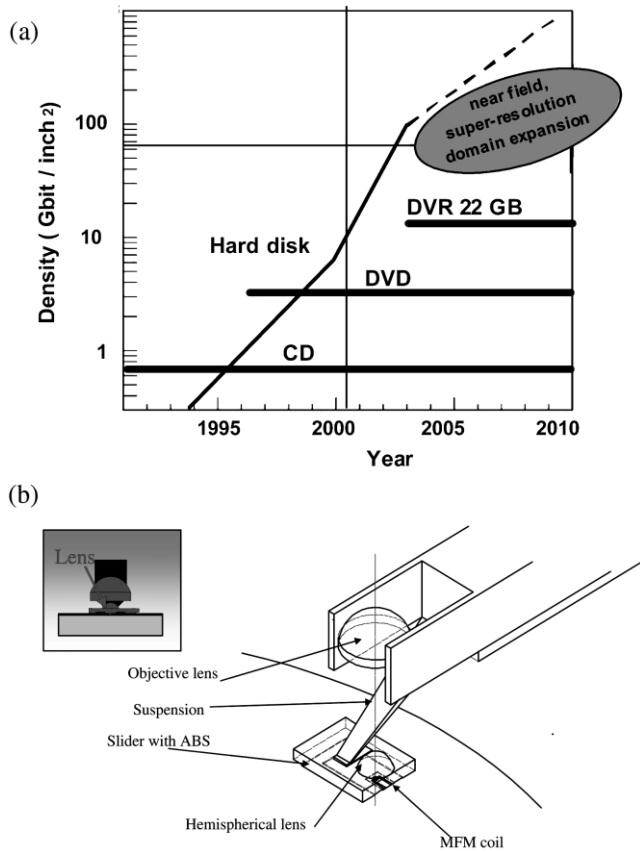


Fig. 8. (a) The development of data densities of various storage media over the last years, and future trends. New technologies like Near Field, super resolution and domain expansion will enable the next jump of capacity to approximately 100 GB per CD sized (120 mm) disk [18]. (b) Schematic drawing of integrated magneto-optical slider with MFM coil for NA=0.85 [18].

devices will have approximately a 20-fold higher capacity than digital versatile disks (DVD), or approximately 100 GB per 12-cm diameter compact disk (CD). One approach to meet the demand for high data capacity of optical disks is the use of flying head technology, which is the method used in magnetic storage (Fig. 8b) [18]. The key feature to differentiate the new generation from the previous ones will be the very small free working separation (between 50 nm and 5  $\mu\text{m}$ ) between the objective lens or magnetic modulation device and the storage disk. The straightforward way to achieve such a small separation is to mount the lens on a slider, which flies above the spinning disk at a constant height on a hydrodynamic air bearing, without needing a complicated servo system [18]. In those conditions, a wear resistant layer is needed to protect the disk and slider from head crash [19].

As for magnetic disks, also next generation optical storage disks based on this technology will need to use amorphous carbon as protective coating [18,19]. However, carbon coatings for magnetic storage disks do not need to transmit light. On the other hand, for optical

storage, the carbon films must also be transparent at the recording wavelength of  $\sim 400$  nm. This would require films with at least  $\sim 3$  eV gap. But, since the target is to let the blue laser line go through the carbon coating, what really matters is the film transmittance rather than its optical gap. One way to increase the transmittance for a lower gap is to decrease the film thickness. The stress must be minimized as it can affect the magneto-optic response of the recording layers. In addition, the energy flux during the growth onto plastic substrates of low thermal conductivity must be controlled in order to prevent over-heating and preserve the substrate integrity. Finally, the adhesion of transparent carbon layers to both the glass or plastic of the slider and upper layers of the disk (e.g. an acrylic cover layer) has to be considered. ta-C and ta-C:(H) are thus being investigated as slider and head overcoats [19]. This, in principle, parallels the efforts for the development of the magnetic storage disks overcoats. On the other hand, the much bigger flying height required in optical storage disks with respect to magnetic disks relieves the constraint of ultra-thin thickness on the overcoat. Thus, the most challenging scenario is found in HDD coating, which is the main focus of this paper.

## 5. Ultra-thin carbon films characterization

Finding reliable characterization tools for ultra-thin carbon layers down to a few atomic layers thickness is one of the most decisive factors for technology development and production [51–65]. The carbon performance is judged in terms of its coverage, lubricant compatibility and mechanical hardness. The mechanical hardness is directly related to the fraction of C–C  $\text{sp}^3$  bonds and the carbon film density. The intrinsic coverage, as we will be discussing in Section 5.1, can be as well related to the fraction of energetic ions, which is also indirectly linked to the  $\text{sp}^3$  fraction and density. The factors affecting the lubricant compatibility are not fully known [75,76].

Rather than reviewing all possible techniques suitable to assess carbon films, here are highlighted some recent results obtained by using atomic force microscopy, Raman spectroscopy, X-ray reflectivity (XRR) and surface acoustic waves (SAWs) based methods on thin ( $< 100$  nm) and ultra-thin ( $< 10$  nm) films.

### 5.1. Roughness evolution

Roughness evolution studies by atomic force microscopy can be used to determine the minimum thickness for which a carbon film can be grown continuous and pin-hole free. This parallels the direct testing performed by chemical, mechanical and spectroscopic methods to assess the coverage and corrosion protection of the overcoats [43,75]. The knowledge of the surface evolution mechanism of a certain class of carbon films, allows

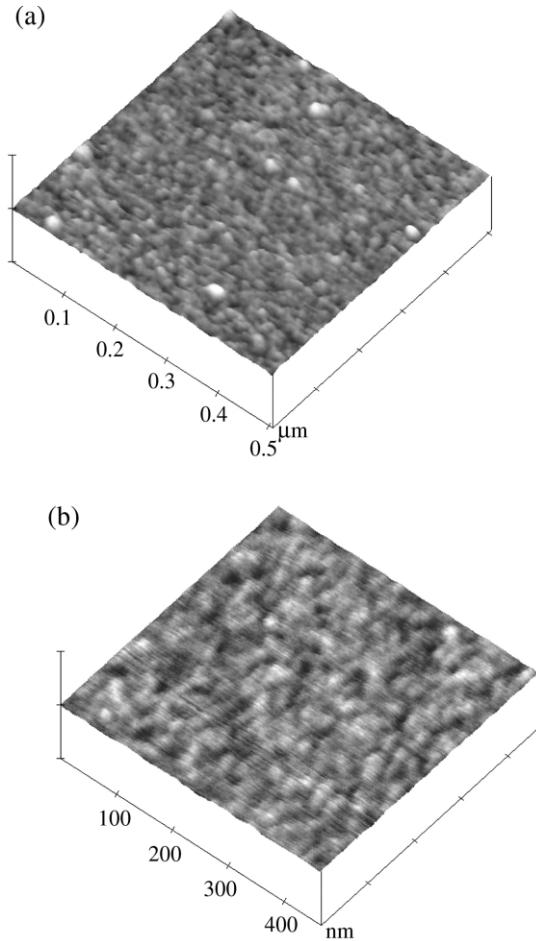


Fig. 9. AFM pictures of ta-C films, (a)  $\sim 1$  nm thick; (b)  $\sim 70$  nm thick.

one to know if the loss of continuity in ultra-thin films is an intrinsic and unavoidable problem related to the nature of the deposited film, or if it is a technical problem, which could be improved with better process conditions. Here we show how surface roughness by AFM allows to explain the ultra-smoothness of ta-C films.

If  $h$  is the film thickness and  $R$  the roughness, the film is continuous if  $h - R$  remains sizeable as  $h$  decreases. The roughness evolution of a film can generally be described by the fractal scaling laws [66], in which  $R$  scales as

$$R \sim \ell^\alpha f(t/\ell^{\alpha/\beta}) \quad (4)$$

Here  $t$  is the deposition time (assuming a constant deposition rate),  $\ell$  is the length scale, i.e.  $\ell \times \ell$  is the window size where  $R$  is measured, with  $\ell \leq L$  the size of the sample.  $f(u)$  is a scaling function of the argument  $u = t/\ell^{\alpha/\beta}$ . For small times, that is  $u \ll 1$ , then  $R \sim t^\beta$  and the heights at different surface sites are independent.

As time increases, the heights at different sites become correlated. When the correlations are significant, the roughness saturates at a constant value  $R_{\text{sat}}$ .  $\alpha$  is called the roughness exponent ( $0 \leq \alpha \leq 1$ ).  $\beta$  is called the growth exponent [66]. The exponents  $\alpha$  and  $\beta$  uniquely characterize how the surface evolves with the length scale  $\ell$  and the time  $t$ . Their values define different growth mechanism universality classes [66,67]. For example, in random deposition the particles stick immediately where they land on a surface and  $\beta$  is 0.5, while  $\alpha$  is undefined. In the random deposition with surface diffusion, the particles do not stick immediately, they can diffuse to a nearby valley site with lower height. This mechanism gives  $\beta = 1/3$  and  $\alpha = 1$ . For ballistic deposition (with no diffusion), lateral sticking is also allowed, creating overhangs, in contrast to the random deposition model. This gives fractal exponents of  $\beta = 0.5$  and  $\alpha = 2/3$ .

Fig. 9 shows the AFM pictures of 1 and  $\sim 70$  nm thick ta-C films. The surface is continuous and is characterized by uniformly distributed features.

Fig. 10 plots the roughness as a function of the film thickness for two sets of ta-C films, deposited on a lab scale S-bend FCVA [49] and a production near process HCA source [50]. The roughness is constant ( $R \sim 0.12$  nm) for every sample [47]. The roughness values are in agreement with previous reported data on thicker films [68]. The roughness is thus always much lower than the film thickness, so that  $h - R$  is positive even for 1-nm films and no pin-holes are expected. Note that the apparent roughness increase for low thickness in the FCVA films is due to the higher roughness of the Si substrate ( $\sim 0.2$  nm) used for these films with respect

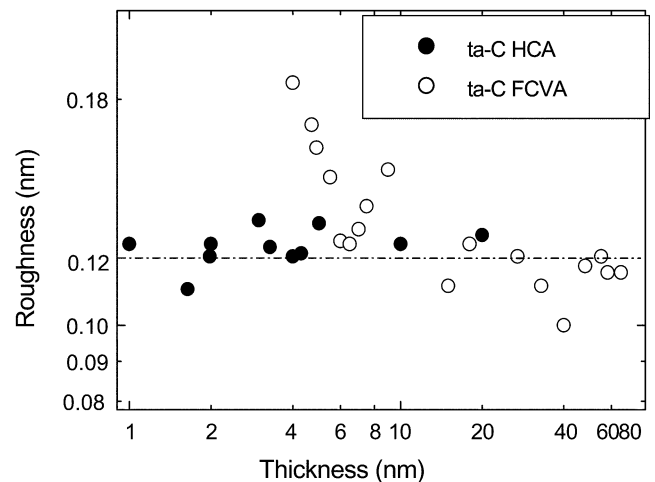


Fig. 10. Roughness evolution as a function of film thickness for ta-C films on Si deposited by FCVA and HCA. Note that the roughness increase of the thinnest FCVA ta-C films is a substrate effect due to the slightly higher roughness of the Si substrate used for these films.

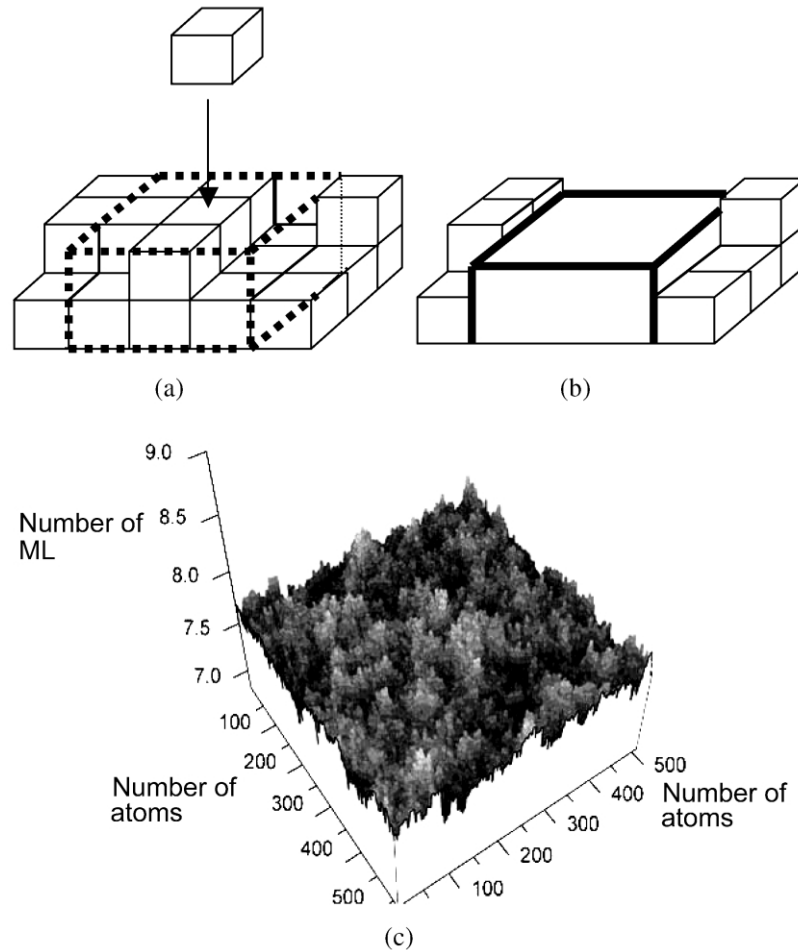


Fig. 11. (a and b) Model used in the Monte Carlo simulations. (a) The energy of an incident ion dissipates in a thermal spike volume, dot line. (b) This causes local melting and flattens the surface locally. (c) Simulated surface after thermal spikes cause a flattening to second neighbors of the incident ion. The scaling exponents are:  $\beta \sim 0.1$  and  $\alpha \sim 0.32$ .

to the lower roughness substrate ( $\sim 0.1$  nm) used for the HCA films. This shows the smoothing effect of the ta-C films even on a relatively smooth substrate, such as the Si used for the FCVA films.

Being the roughness constant with film thickness, the growth exponent  $\beta$  is zero [47]. It was also shown that  $\alpha \sim 0.4$  [47]. These exponents do not match any of the existing universality classes of growth mechanisms previously described [66].

Growth exponents  $\beta \sim 0$  generally arise from surface diffusion and relaxation [69]. To find the origin of this smoothness and investigate the growth mechanism of the ta-C surface, Monte Carlo simulations were performed [47].

ta-C grows from energetic carbon ions. The generally accepted model for  $sp^3$  formation and ta-C growth is sub-plantation [20]. In this model two basic mechanisms are assumed to produce the  $sp^3$  bonding: (i) the high temperature associated with the ‘thermal spike’, due to

the excess of energy dissipated by the impinging carbon ion within the local structure. (ii) The incorporation of carbon atoms in sub-surface positions causing local densification. The thermal spike is considered responsible for the surface relaxation during ta-C growth [47]. When the incident ion penetrates the outer atomic layer of the film and goes to the sub-surface layer, its energy is dissipated within a thermal spike volume. This induces the material to melt locally and behave as a liquid. The surface area of the thermal spike becomes locally flat. The only parameter in the Monte Carlo simulations is the number of nearest neighbors affected by the thermal spike.

Fig. 11a and b show a schematic representation of the surface before and after the local melting effect. Up to three nearest neighbors were considered.  $\beta$  was found to be between 0.08 (first neighbors) and 0.15 (third neighbors). The roughness exponent  $\alpha$  slowly increases as the number of nearest neighbors considered increases,

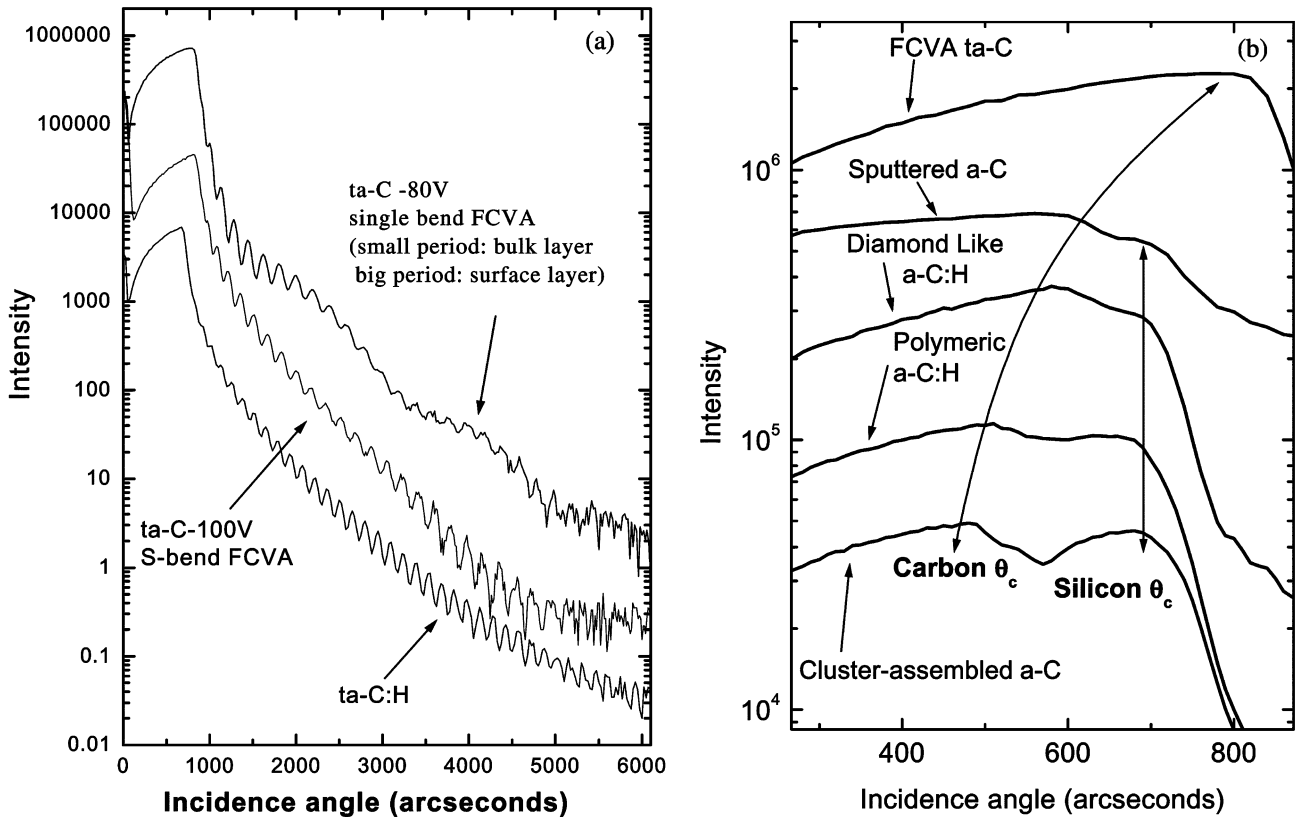


Fig. 12. (a) XRR profiles for single bend and S-bend-FCVA grown ta-C films and for a representative ta-C:H film grown by ECWR [21]. The clear double fringe period in the single bend FCVA film indicates layering. (b) XRR profiles for carbon films with density ranging from lower to higher than the Si substrate density. The film critical angle moves with increasing film density. For films denser than Si, such as ta-C films, only the film critical angle is observed.

being between 0.26 (first neighbors) and 0.36 (third neighbors), (Fig. 11c). Thus, this model is able to explain the observed growth exponents. This model could be extended to hydrogenated ta-C (ta-C:H), which possess as well a very low roughness (0.13 nm).

### 5.2. X-ray reflectivity

XRR is a fast and non-destructive technique for the characterization of density, thickness, roughness and layering of carbon films [21,70].

For X-rays the refractive index in solids is slightly smaller than unity, so that total external reflection occurs at low angles of incidence. As the incidence angle  $\theta_i$  increases above a critical angle  $\theta_c$ , X-rays start to penetrate into the film [71,72]. For an ideally smooth surface the reflected intensity falls off as  $(2\theta)^{-4}$ , as predicted by Fresnel's equations. For a real sample the fall off is more rapid, because of the surface roughness, which scatters X-rays out of the specular beam. For a thin layer, of refractive index  $n_1$ , deposited onto a bulk substrate, of refractive index  $n_2$ , reflections at the different interfaces will cause interference. There will be constructive interference when the path difference

between the reflected beams is  $\delta = (m + 1/2)\lambda$  or  $\delta = m\lambda$ , where  $m$  is an integer, for  $n_1 < n_2$  and  $n_1 > n_2$ , respectively. The period  $\Delta\theta$  of the fringes gives the carbon film thickness; for  $\theta_i \gg \theta_c$ :

$$d \approx \frac{\lambda}{2\Delta\theta}. \quad (5)$$

In the case of a multilayer the structural periodicity results in the presence of Bragg peaks in the reflectivity curve.

Fig. 12a plots typical specular reflectivity curves for ta-C films, deposited by single and S-bend FCVA, and ta-C:H films. For the S-bend FCVA ta-C and the ta-C:H film one dominant fringe period can be seen, showing that these films are essentially single layered. The interference fringe period gives a direct measure of the film thickness, the thinner films having longer period fringes. The single bend ta-C film shows also a second set of longer period fringes, which indicate the presence of a surface layer. Indeed, to a closer inspection, the S-bend FCVA ta-C film also presents a very faint second set of fringes with an even bigger period, indicating a much smaller, but non-negligible, surface layer.

XRR is thus also a powerful tool to check the cross-sectional layering of films. Analysing a wide variety of films grown under different conditions it was found that extremely uniform or layered films can result even from the same deposition system [21].

The density of amorphous carbon films is obtained from the critical angle. Carbon films relevant for magnetic storage disks contain three basic elements, C, N and H. The density is related to the critical angle by [21,70]

$$\rho = \frac{\pi^2 c^2 \varepsilon_0}{3 \lambda^2 N_A e^2} M_C m \theta_c^2 \frac{11X_C + 13X_N + 1}{5X_C + 6X_N + 1} \quad (6)$$

where  $X_H = 1 - X_C - X_N$  is the H atomic fraction,  $X_C$  and  $X_N$  are the C and N atomic fractions.  $e$  is the electron charge,  $m_e$  is the electron mass,  $N_A$  is the Avogadro number,  $c$  is the velocity of light,  $\varepsilon_0$  is the dielectric permittivity of vacuum,  $\lambda$  the X-ray wavelength and  $M_C$  the carbon molar mass. Note that the dependence on the H content is quite weak in the usual range  $X_H = 10\text{--}50\%$  (e.g.  $\rho = 2.3 \text{ g/cm}^3$  if  $X_H = 0.1$  and  $2.16 \text{ g/cm}^3$  if  $X_H = 0.5$ , with  $X_N = 0$ ,  $\theta_c = 720''$  and  $\lambda = 1.3926 \text{ \AA}$ ), so an approximate density evaluation can be obtained by neglecting the H content. Similarly, an estimate of the density can also be performed considering the films as made of carbon only, even if N is present. However, only by knowing the exact film composition the most accurate results can be derived.

The use of the critical angle for density measurement is exemplified in Fig. 12b for carbon films a few tens of nanometer thick on a Si substrate. Some films, such as ta-C:Hs, have a density (and therefore a critical angle) which is similar to or just smaller than the Si substrate density ( $2.33 \text{ g/cm}^3$ ), so that the Si critical angle is seen, and not that of the film. The presence of the film only acts as a perturbation on the shape of the critical angle and a simulation of the reflectivity curve is needed to extract the density. In the case of films with very low density (e.g. porous carbon films, or some a-C:H and a-C films) a double critical angle is distinguishable (Fig. 12b). This allows a direct determination of the density from the reflectivity curve. Finally, if the film consists of a bulk layer denser than the Si, the critical angle is determined by the film. This is typically the case for ta-C films (Fig. 12b). For ta-C films a single critical angle is observed and densities up to  $3.26 \text{ g/cm}^3$  are obtained for a 70 nm thick  $\sim 88\%$   $\text{sp}^3$  film from the S-bend FCVA [21]. The general density/ $\text{sp}^3$  relation for carbon films presented in Section 2 (Eq. (1) Fig. 7) was derived by XRR [21].

Fig. 13 shows XRR data on ultra-thin ta-C films, indicating the ability of XRR to measure films in the sub 10 nm range. Indeed, ta-C films have been measured down to a thickness of approximately 1 nm [53,70,73,74]. Unlike the case of thicker films, for ultra-

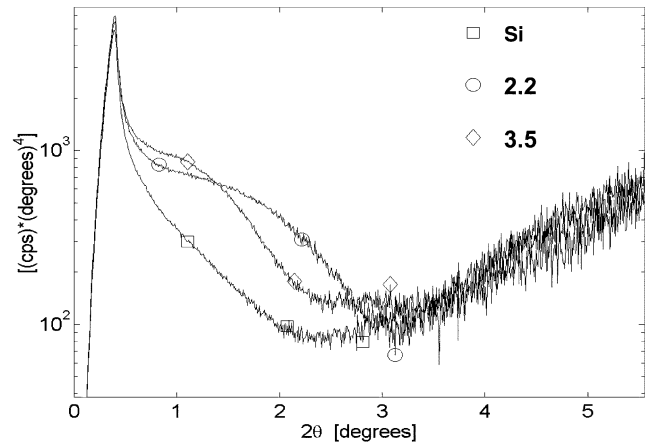


Fig. 13. XRR profiles for ultra-thin ta-C films on Si compared to the bare Si substrate, showing how XRR can discriminate between film and substrate even for extremely small films' thickness.

thin carbon films the critical angle is not strongly influenced by the film density. This is because the evanescent wave reaches the silicon substrate below the critical angle and the substrate density determines the critical angle. Only for ta-C films on silicon over approximately 20-nm thickness the critical angle can be used reliably to measure the near-surface density. Although the density influences the fringe contrast, the film interface width also influences the contrast. On the other hand, the film density does affect the position of the fringe maximum. So an overall fit of the reflectivity profile is necessary to derive the film properties. A degree of uncertainty thus remains in the determination of the film density for these ultra-thin layers, whilst the thickness is precise to 0.1 nm [73]. A density of  $\sim 2.6/2.8 \text{ g/cm}^3$  is measured even for ultra-thin ta-C films. This agrees with the corrosion resistance, which is found to be maintained down to the nanometer scale [43,74]. Note as well that the structure of the ultra-thin ta-C films resembles that of the thicker ta-C, with a scaling of the bulk layer thickness, but not of the surface and interface layers (which are in the sub-nanometer range both in thick and thin films).

Finally, although we mainly discussed results for carbon films on Si, XRR is successfully applied for carbon overcoats deposited on disk [57,74,77].

### 5.3. Surface acoustic waves

When the film thickness is considerably lower than 1  $\mu\text{m}$  and the substrate is softer than the film, standard experimental procedures, as well as nano-indentation, are unable to reliably determine the elastic constants of the film. The difficulties of nano-indentation arise from the need to use an indentation depth less than 10% of the film thickness and its high sensitivity to the substrate when measuring hard films on a soft substrate. Nano-

indentation actually measures the hardness, but the reduced Young's modulus  $E' = E/(1 - \nu^2)$  can be derived by an Oliver–Pharr [78,79] analysis of the indentation curve, so that  $E$  itself can be found if a value for the Poisson's ratio,  $\nu$ , is assumed. The difficulties of this method are clear in that while the hardness values of ta-C are found to be between 60 [79,81] and 90 GPa [80], the  $E'$  values vary more widely, from 400 [79,81] to 1100 GPa [80]. Various strategies have been proposed to improve the Oliver–Pharr analysis of the nano-indentation data [80]; however, it is very unlikely that they can work down to 1-nm film thickness.

More convenient approaches are based on laser spectroscopic methods related to the propagation properties of long wavelength acoustic phonons (SAWs): surface Brillouin scattering (SBS), exploiting thermally activated SAWs [22,48,82,83] and laser-induced SAW techniques (LAW) exploiting SAWs excited by laser irradiation [51,84]. Both SAW based methods offer the possibility of non-destructive measurements of the film elastic constants. Both techniques are non-destructive: they measure the velocity of SAWs, and derive from it the film properties. There are, however, significant differences in the way they operate. While SBS relies on thermally excited SAWs, LAW induces them by laser pulses, and allows significantly faster measurements. LAW analyses pulse propagation in the time domain, while SBS is a spectroscopic technique. LAW measures propagation in the megahertz to hundreds of megahertz frequency range, while SBS operates in the tens of gigahertz range, and is therefore intrinsically more sensitive to perturbations by thin films. On the other hand, velocity measurements by LAW are more precise, and these two features tend to compensate.

The ability of SBS and LAW to measure thin and ultra-thin ta-C films was assessed by performing a round-robin test [85]. The results of the test showed a good correlation between the Young's moduli measured by SBS and LISAW. This confirms the ability of SAW based techniques to assess the Young's modulus in a thickness range not attainable by conventional techniques. Also, this allows a validation of the LAW data by the more precise SBS measurements. This is crucial since SBS requires an average of a week to perform the measurements necessary to extract a film's elastic constants, whilst LAW can perform the same analysis in a few minutes. Even though a value for the Poisson's ratio has to be guessed for LAW, this does not significantly affect the final  $E$  values [85].

Fig. 14 plots the evolution of the Young's moduli of ta-C films deposited by HCA as a function of the thickness. The evolution of film properties with thickness will be discussed in Section 6.

#### 5.4. Resonant Raman spectroscopy

All carbons show common features in their Raman spectra in the 800–2000/cm<sup>-1</sup> region, the so-called G

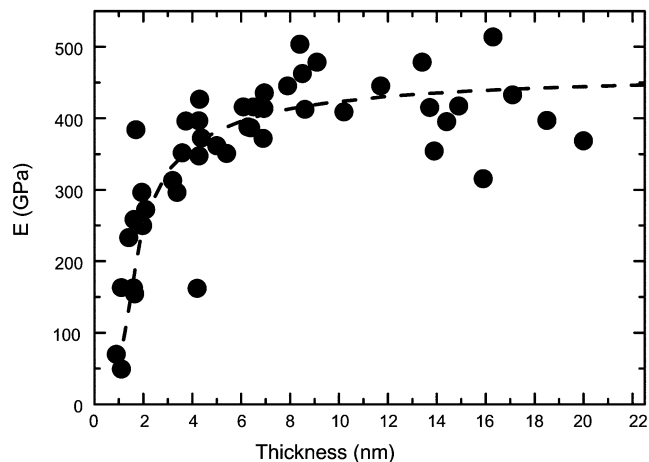


Fig. 14. Young's modulus vs. film thickness for a series of HCA ta-C films, measured by LAW. The dashed line plots Eq. (9), see Section 6.

and D peaks, which lie at approximately 1560 and 1360/cm<sup>-1</sup>, respectively, for visible excitation and the  $T$  peak at approximately 1060/cm<sup>-1</sup>, seen only in UV excitation. Except for UV excitation, the Raman spectra are dominated by the sp<sup>2</sup> sites, because the excitation resonates with  $\pi$  states. The G and D peaks are due to sp<sup>2</sup> sites. The G peak is due to the bond stretching of all pairs of sp<sup>2</sup> atoms in both rings and chains. The D peak is due to the breathing modes of sp<sup>2</sup> atoms in rings [86,87]. The  $T$  peak is due to the C–C sp<sup>3</sup> vibrations [86,88,89].

A phenomenological three-stage model was developed in Refs. [86,88,23] to interpret the Raman spectra of any amorphous carbon measured for any excitation energy. The evolution of the carbon system from graphite to nc-G, a-C and finally ta-C is represented by an amorphisation trajectory, evolving over three stages (Figs. 6 and 15). The Raman spectra fundamentally depend on the following parameters:

- clustering of the sp<sup>2</sup> phase
- bond disorder
- presence of sp<sup>2</sup> rings or chains and
- the sp<sup>2</sup>/sp<sup>3</sup> ratio.

Under some circumstances, such as if the deposition temperature is varied or if the films are thermally annealed, the sp<sup>2</sup> configuration is not unique and it can vary independently of the sp<sup>3</sup> content. In this case, for a particular sp<sup>3</sup> content and excitation energy, we can have a number of different Raman spectra, or, equivalently, similar Raman spectra for different sp<sup>3</sup> contents. This non-uniqueness was called hysteresis [86], since by following an ordering trajectory, from high sp<sup>3</sup> to low sp<sup>3</sup> material, the G-peak position and  $I(D)/I(G)$  do not necessarily follow the same trajectory defined by the amorphisation trajectory (Fig. 15b).

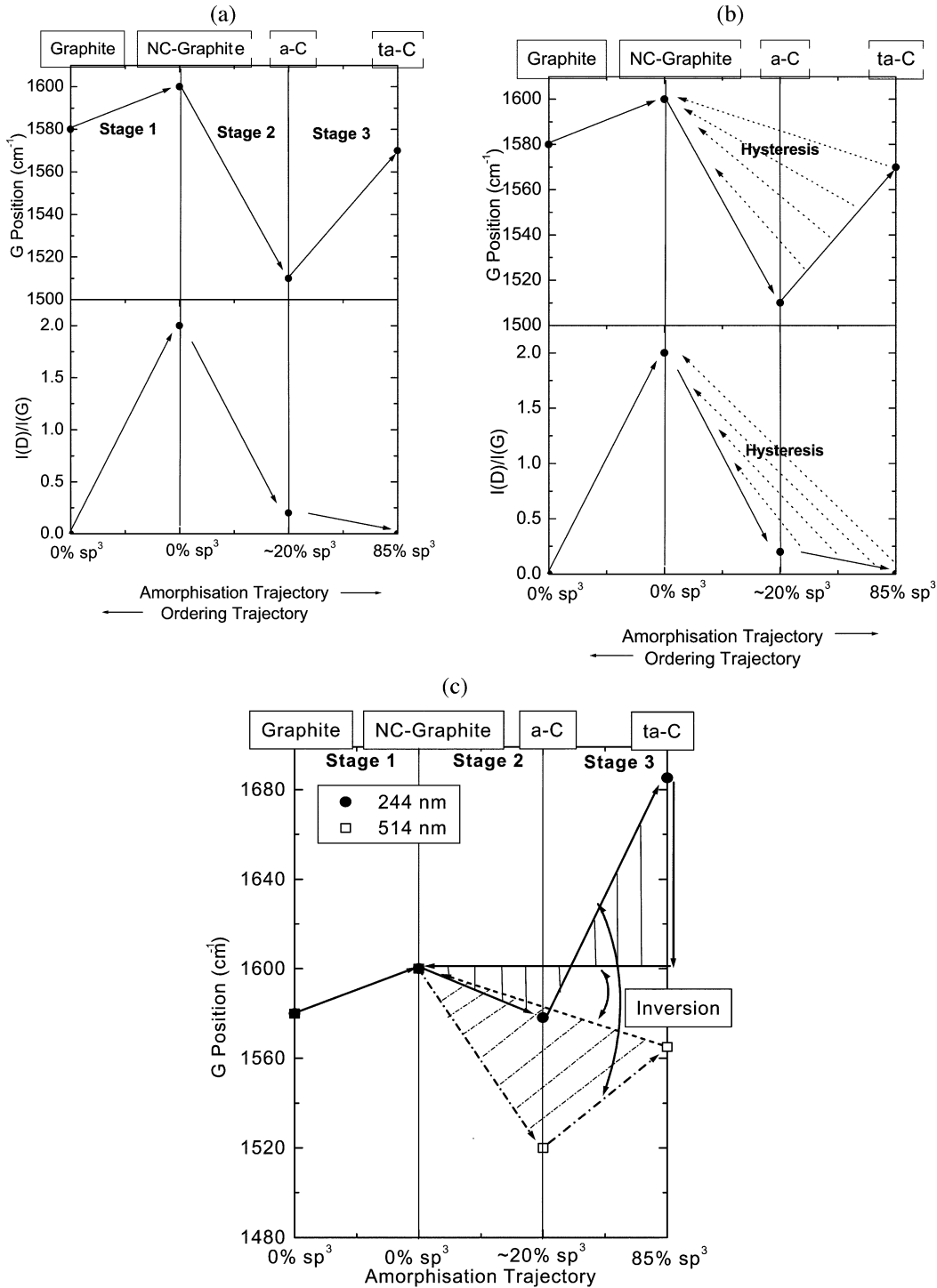


Fig. 15. Three-stage model of the variation of the Raman G position and the D to G intensity ratio,  $I(D)/I(G)$ , with increasing disorder, for visible excitation (a and b) and for multiwavelength excitation (c). The dotted left-pointing arrows in (b) mark the non-uniqueness region in the ordering trajectory. (c) Amorphisation trajectory, showing the possibility of non-uniqueness in stages 2 and 3 for two typical wavelengths (514.5 and 244 nm). The regions span by hysteresis at 514.5 and 244 nm are evidenced by lines. Note the trend inversion, with the highest shift Vis  $\rightarrow$  UV for samples having the least ordered  $sp^2$  phase.

This is relevant for magnetic disk coating, since high temperature deposition and N incorporation both favour the clustering of the  $sp^2$  phase and this clustering not necessarily follows the  $sp^3$  to  $sp^2$  conversion. We thus

expect non-uniqueness in the relation between visible Raman spectra and the film properties.

On the other hand, the G-peak FWHM is a measure of disorder and increases continuously as the disorder

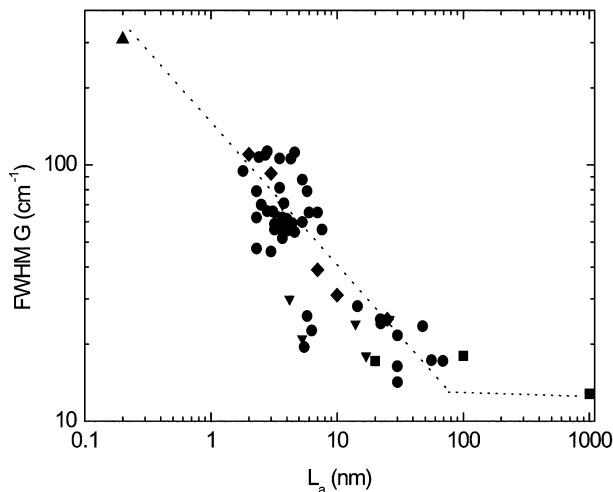


Fig. 16. Variation of G-peak FWHM with decreasing  $sp^2$  grain size  $L_a$  for visible excitation [23]. The line is a guide to the eye. The FWHM G saturates at  $\sim 12/cm^{-1}$  for high grain size graphitic samples. The trend at any excitation wavelength resembles the visible Raman trend, but the absolute values of FWHM decrease for decreasing excitation wavelength.

increases (Fig. 16). The FWHM is thus uniquely related to the  $sp^2$  clustering. Indeed, although graphite and ta-C exhibit similar G-peak positions for visible excitation (Fig. 15), the G-peak FWHM in ta-C is much bigger than graphite (Fig. 16) and as such easily discriminates between the two materials.

By using different wavelengths and by analysing the behaviour of the Raman parameters as a function of the excitation wavelength, additional important information on the internal structure of the carbon system becomes available [23,86,88]. The most useful parameter derived by such an analysis is the dispersion of the G peak. Ref. [88] showed that the G-peak positions change in a roughly linear way as a function of the excitation energy. The G-peak dispersion was thus defined as the slope of the line connecting the G-peak positions measured at different wavelengths [88]. For industrial applications we want to use the minimum number of excitation wavelengths. It can thus be assumed that the variation of the G-peak position is perfectly linear with excitation wavelength and the G-peak dispersion can be conveniently defined as

$$G_{Disp} = \frac{G_{Pos}(UV) - G_{Pos}(Vis)}{\Delta\lambda} \quad (7)$$

where  $\Delta\lambda = 514.5 - 244 \text{ nm} = 270.5 \text{ nm}$  for typical UV and Vis wavelengths.

The G-peak position increases as the excitation wavelength decreases, from visible to UV. The dispersion rate increases with disorder. The G peak does not disperse in graphite itself, nc-G or glassy carbon [88]. The G peak only disperses in more disordered carbons,

where the dispersion is proportional to the degree of disorder [88]. This allows us to solve the non-uniqueness problem. The G-peak dispersion separates the materials into two types. In materials with only  $sp^2$  rings, the G-peak dispersion saturates at a maximum of  $\sim 1600/cm^{-1}$ , the G position in nc-G. In contrast, in those materials also containing  $sp^2$  chains, particularly ta-C and ta-C:H, the G peak continues to rise past  $1600/cm^{-1}$  and can reach  $1690/cm^{-1}$  at 229-nm excitation in ta-C. Thus, ta-C has the largest dispersion, followed by ta-C:H and polymeric a-C:H.

In case of non-uniqueness, following an ordering trajectory, as for Fig. 15b and c, in visible Raman spectra the G-peak position tends to increase going from stage III to stage II. For UV Raman spectra, however, clustering induces a decrease of the G-peak position when moving from stage III to stage II, Fig. 15c. These opposite trends in visible and UV Raman can be used to solve the non-uniqueness problem. If the G-peak positions of two carbon samples are similar for 514.5-nm excitation but differ in the UV, then the  $sp^2$  clustering is higher in the sample with the lower G-peak dispersion.

A clear demonstration of this behaviour can be seen in Fig. 17. The G-peak positions of the visible and UV Raman spectra are plotted against N content for the series of (t)a-C:N films. The N content ranges from 0 to 35 at.%. The linear decrease of the UV G-peak position with increasing N content contrasts with the very weak change of the G peak measured by visible Raman spectroscopy. However, if the G-peak dispersion is used, a unique relationship with the N content is found, Fig. 17b.

Fig. 18 shows how the G-peak dispersion correlates with the density for a variety of different carbon films used in hard disk coating with or without N or H [65].

The scratching resistance is a method used in the hard disk industry to assess the mechanical properties of ultra-thin carbon overcoats. It is performed by using an AFM with diamond tips [55,77]. Using image subtraction, scratches down to a residual depth of 0.1 nm can be evaluated, hence enabling the study of the very beginning of plastic deformation. The scratch resistance is defined by the ratio of the applied loading force and the cross-sectional area of the scratches. The scratch resistance directly relates to the shear modulus and hardness of the carbon overcoats. The elastic constants of amorphous carbons scale with the  $sp^3$  fraction and thus with the density, Section 2, Eqs. (1)–(3). The G-peak dispersion should thus directly correlate with the scratching resistance. This is clearly shown in Fig. 19a and b, where a linear relation between the G-peak dispersion and the scratching resistance of two sets of magnetron sputtered a-C:N and arc deposited ta-C:N is shown. Note that for the a-C:N the scratching resistance increases with the N content, whilst for ta-C:N it

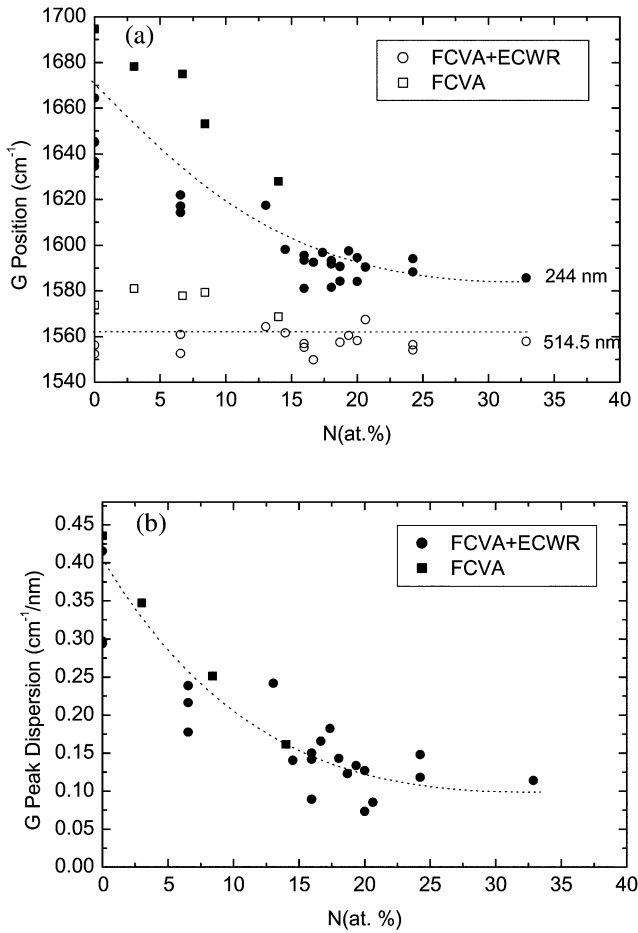


Fig. 17. (a) G-peak position vs. N content for 244 and 514-nm excitation for (t)a-C:N samples deposited by FCVA+ECWR and FCVA alone. (b) Dispersion of G peak vs. N content. The lines are guides to the eye.

decreases, as we expect from the general trends described in Section 2.

The analysis of the G peak at different wavelengths also provides the trends in the G peak FWHMs, which are similar to the trend in the G-peak dispersion, even though more scattered, each being single wavelength data.

Resonant Raman spectra can be measured for ta-C films down to  $\sim 1$ -nm thickness [54]. Fig. 20a plots the G dispersion and FWHM measured at 514.5 and 244 nm as a function of the film thickness on two batches of ta-C films of increasing thickness, one deposited by a lab scale S-bend FCVA, the other in a production near process environment by HCA. In both cases the Raman parameters strongly decrease below 10 nm. This directly correlates with the data on Young's modulus vs. thickness reported in Fig. 14 for HCA films and in Ref. [48] for S-bend FCVA films, the latter reaching  $E \sim 760$  GPa. Indeed, combining the Raman and surface acoustic data we can obtain a linear relation between G-peak disper-

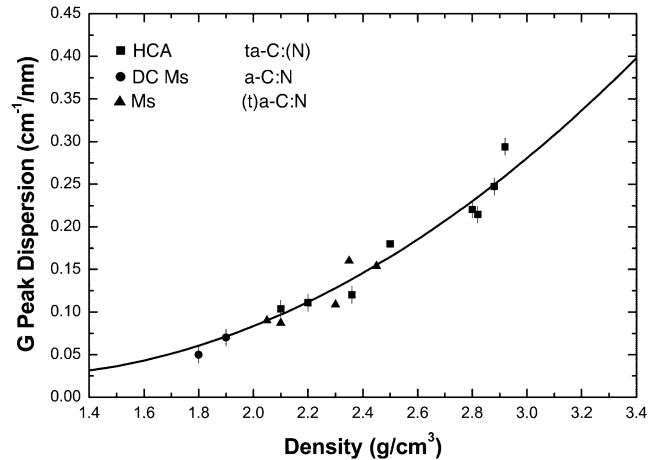


Fig. 18. G-peak dispersion as function of the mass density for different carbon nitride films used for hard disk coating, deposited by HCA, biased magnetron sputtering (Bias MS) and DC magnetron sputtering (DC MS). A clear correlation over a large density region is seen.

sion and Young's modulus for ta-C films of increasing thickness, Fig. 20b:

$$E \text{ (GPa)} = 1936.6 \times G_{\text{Disp}} (\text{cm}^{-1}) - 146.8 \quad (8)$$

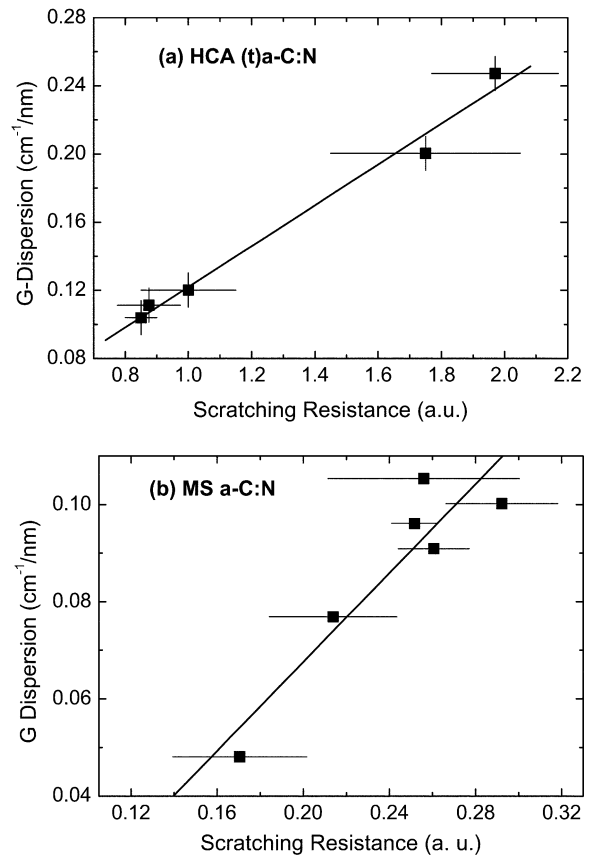


Fig. 19. G-peak dispersion vs. scratching resistance for MS sputtered and HCA (t)a-C:N films used for hard disk coating.

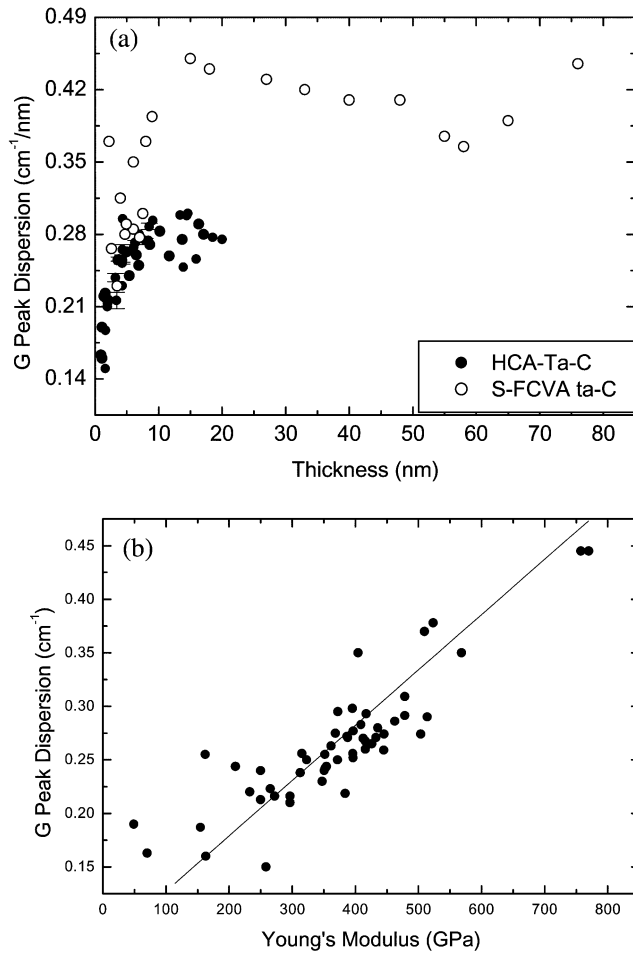


Fig. 20. (a) G-peak dispersion vs. thickness for a set of S-bend FCVA ta-C films deposited by a lab scale source and of production near process HCA ta-C films. (b) G-peak dispersion vs. Young's modulus for ta-C films of increasing thickness, deposited either by HCA or FCVA and measured by LAW. Both sets of samples fall on the same line, as expected.

In principle this relation could be used in conjunction with Eqs. (1)–(3) to derive the density and the  $sp^3$  fraction; however, the results are likely to be underestimated and qualitative, since thinner and softer films are not equivalent to a thin slice of a bulk film with the same density and  $sp^3$  [48] (Section 6).

Fig. 20 shows that the G-peak dispersion ranges from 0.45 to 0.2/cm<sup>-1</sup> nm for S-bend FCVA films, whilst it ranges from 0.28 to 0.1/cm<sup>-1</sup> nm for HCA ta-C films. This means that the lab scale S-bend FCVA ta-C can reach higher densities,  $sp^3$  content and mechanical properties than the production line HCA ta-C, for each thickness. However, production line HCA films have better uniformity over large areas and lower macroparticles density [50]. The higher instantaneous deposition rate of HCA films also increases the temperature of the  $sp^3$  to  $sp^2$  transition with respect to S-bend FCVA films

[90]. This is again important since the process temperature for hard disk deposition is  $\sim 200$  °C.

## 6. Evolution of ta-C properties with thickness

Figs. 14 and 20a allow some interesting conclusions on the thickness evolution of ta-C properties. The density,  $sp^3$  fraction and Young's modulus all decrease for films below 8-nm thickness [48]. However, there are distinct trends. The XRR density of a 2.2-nm ta-C film, 2.8 g/cm<sup>3</sup>, corresponds, by using Eq. (1), to  $\sim 60\%$   $sp^3$  content, similar to that found by direct electron energy loss spectroscopy measurements ( $\sim 45\%$ ) [48]. In contrast, its Young's modulus ( $\sim 100$  GPa) would correspond to a much lower density of 1.9 g/cm<sup>3</sup> and an  $sp^3$  fraction of  $\sim 0$ , if Eqs. (1)–(3) are applied. This is general. The  $sp^3$ -density correlation of bulk ta-C of Eq. (1) still holds for ultra-thin films. However, the ultra-thin films are softer than bulk films (60–70 nm thick) of the same density, so Eqs. (2) and (3) do not hold. This conclusion bears fundamental implications for the magnetic disk coating applications of DLCs. It explains why ta-C films can maintain their corrosion protection properties down to 1-nm thickness, even if their mechanical properties are much softer than bulk ( $>10$  nm) films. The softening of the mechanical properties of ultra-thin films is a size effect and does not imply a strong density and  $sp^3$  decrease, nor a change in the surface smoothness. Indeed, Section 5.1 showed that the roughness is constant for decreasing film thickness.

Thus, the first thickness reduction effect is that, for a given density and  $sp^3$  content, the mechanical properties of an ultra-thin films are softer than what expected for the same film if it was thick.

The second effect is that the density and  $sp^3$  fraction of ultra-thin films are, however, smaller than the maximum reported for bulk films. This can be understood if one considers the cross-sectional structure of ta-C films [21]. The films consist of three layers, an outer layer, a middle 'bulk' layer and an interfacial layer. The outer surface layer is approximately 0.5 nm thick and is more  $sp^2$  like. Its thickness corresponds to the carbon ion range. There is also an interfacial layer between the C and the Si substrate, where ion mixing creates C–Si bonding. Since the deposition conditions are constant during film growth, the thickness of the surface and interface layers is roughly independent of the total film thickness [21]. Thus, for thinner films, the thickness of the middle 'bulk' layer decreases, but the nature of the surface layer (and thus the roughness) should not change much with thickness, for a given ion energy. The surface layer is also softer than the bulk film. This is also true for the interface layer, as C–Si bonds are softer than C–C bonds. This explains the quick decrease of the

mechanical properties once the width of the bulk layer becomes similar to (or smaller than) the interface and surface layers; we expect a strong reduction in the Young's modulus, as observed in Fig. 14.

A simple expression can be derived to describe the evolution of  $E$  vs. thickness:

$$E(z) = E_{\text{Bulk}} - (E_{\text{Bulk}} - E_{\text{csi}})z_{\text{csi}}/z \quad (9)$$

where  $E(z)$  is the Young's modulus at a thickness  $z$ ,  $E_{\text{Bulk}}$  is the Young's modulus of the bulk phase (which can be approximated with  $E$  for  $z > 10$  nm) and  $z_{\text{csi}}$  is the total thickness of the surface and interface layers. For the HCA films in Fig. 14,  $z_{\text{csi}} \sim 1$  nm, whilst  $E_{\text{bulk}} \sim 460$  GPa and  $E_{\text{csi}} \sim 50$  GPa. The line in Fig. 14 is a plot of Eq. (9) and yields an excellent agreement with experimental data, thus confirming this model. A similar equation with  $E$  replaced by  $G_{\text{Disp}}$  can be used to fit the data in Fig. 20a.

In any case, a 2-nm ta-C film still poses a Young's modulus of  $\sim 100$  GPa,  $\text{sp}^3$  content of  $\sim 50\%$  and a  $2.8/2.6$  g/cm<sup>3</sup> density. The smoothness and absence of pin-holes give excellent corrosion resistance down to  $\sim 1$ -nm thickness, as confirmed by direct corrosion tests [43]. Thus, ta-C satisfies all the requirements needed for the ultimate storage density limit of  $\sim 1$  Tbit/inch<sup>2</sup>.

## 7. Conclusions

The status of DLC films to be used as overcoat for magnetic and optical storage disks has been reviewed. The main requirements, such as smoothness, density, corrosion protection have been highlighted. In order to achieve  $\sim 1$  Tbit/inch<sup>2</sup> storage density the challenges is to provide  $\sim 1$ -nm films with suitable properties and to be able to assess these properties in a lab and then on the production line. The main non-destructive measurement techniques for structural evaluation of the carbon overcoats have been presented, showing how they can cope with thin and ultra-thin films. In particular the versatility of Raman spectroscopy for ultra-thin films probing has been underlined. A detailed analysis of the properties of ultra-thin ta-C films has been discussed. These films are able to provide smoothness, corrosion protection and reasonable mechanical properties down to  $\sim 1$ -nm thickness and are thus promising candidates for next generation data storage devices.

## Acknowledgments

The author wishes to thank all the people who allowed the work reviewed in this paper to be performed, in particular the research team of the Mainz IBM STD plant. The author thanks J. Robertson, C. Casiraghi, F. Piazza, R. Ohr, M. Von Gradowsky, C. Shug, H. Hilgers,

D. Schneider, M.G. Beghi, C.E. Bottani, A. Libassi, B.K. Tanner. The author acknowledges financial support from the Royal Society, from the project 'Innovative Reaktoren und In-Situ Analytik für Nano-Schutzschichten' funded by the German Bundesministerium für Bildung und Forschung and the EU project FAMOUS.

## References

- [1] E. Grochowski, D.A. Thompson, IEEE Trans. Magn. 30 (1994) 3797.
- [2] A.K. Menon, in: C.S. Bathia, A.A. Polycarpou, A.K. Menon (Eds.), Proceeding Symposium on Interface Tribology towards 100 Gbits/in<sup>2</sup>, The American Society of Mechanical Engineers, New York, 1999.
- [3] J. Robertson, Thin Solid Films 383 (2001) 81.
- [4] J. Robertson, Tribol. Int. 36 (2003) 405.
- [5] P.A. Goglia, J. Berkowitz, J. Hoehn, A. Xidis, L. Stover, Diamond Relat. Mater. 10 (2001) 271.
- [6] M.F. Doerner, R.L. White, MRS Bull. (September) (1996) 28.
- [7] M.F. Doerner, K. Tang, T. Arnoldussen, H. Zeng, M.F. Toney, D. Weller, IEEE Trans. Magn. 36 (2000) 43.
- [8] R. Wood, IEEE Trans. Magn. 36 (2000) 36.
- [9] R. Wood, IEEE Trans. Magn. 38 (2002) 1171.
- [10] A.K. Menon, Tribol. Int. 33 (2000) 299.
- [11] E. Grochowski, R.D. Halem, IBM Syst. J. 42 (2003) 338.
- [12] J.G. Zhu, Mater. Today July/August (2003) 22.
- [13] E. Grochowsky, Datatech, ICG Publishing, 1998, pp. 11–16.
- [14] A.K. Menon, B.K. Gupta, Datatech 4 (2000) 17.
- [15] Z. Zhang, et al., IEEE Trans. Magn. 38 (1861) 2002.
- [16] J. Gui, IEEE Trans. Magn. 39 (2003) 716.
- [17] B. Zhang, J. Ying, B. Wei, Data Storage 1 (1999) 25.
- [18] C. Morsbach, C. Dubarry, M. Gabriel, et al., IEE Proc. Sci. Measure. Technol. 150 (2003) 203.
- [19] F. Piazza, D. Grambole, L. Zhou, et al., Diamond Relat. Mater., in press.
- [20] J. Robertson, Mater. Sci. Eng. R 37 (2002) 129.
- [21] A.C. Ferrari, A. LiBassi, B.K. Tanner, et al., Phys. Rev. B 62 (2000) 11089.
- [22] A.C. Ferrari, J. Robertson, M.G. Beghi, C.E. Bottani, R. Ferulano, R. Pastorelli, Appl. Phys. Lett. 75 (1893) 1999.
- [23] A.C. Ferrari, S.E. Rodil, J. Robertson, Phys. Rev. B 67 (2003) 155306.
- [24] N. Hellgren, M.P. Johansson, E. Broitman, L. Hultman, J.E. Sundgren, Phys. Rev. B 59 (1999) 5162.
- [25] W.J. Gammon, D.I. Malyarenko, O. Kraft, G.L. Hoatson, A.C. Reilly, B.C. Holloway, Phys. Rev. B 66 (2002) 153402.
- [26] I. Jimenez, R. Gago, J.M. Albella, D. Caceres, I. Vergara, Phys. Rev. B 62 (2000) 4261.
- [27] N.H. Cho, K.M. Krishnan, D.K. Veirs, et al., J. Mater. Res. 5 (1990) 2543.
- [28] H. Tsai, D.B. Bogy, J. Vac. Sci. Technol. A 5 (1987) 3287.
- [29] B. Marchon, M.R. Khan, N. Heiman, P. Pereira, A.S. Lautie, IEEE Trans. Magn. 26 (1990) 2670.
- [30] B. Marchon, N. Heiman, M.R. Khan, A. Lautie, J.W. Ager, D.K. Veirs, J. Appl. Phys. 69 (1991) 5749.
- [31] B. Bhushan, Diamond Relat. Mater. 8 (1985) 1999.
- [32] E.C. Cutiongco, D. Li, Y.W. Chung, C.S. Bhatia, J. Tribol. 118 (1996) 543.
- [33] X. Yun, R.C. Hsaio, B. Bogy, C.S. Bhatia, IEEE Trans. Magn. 33 (1997) 938.
- [34] C.S. Bhatia, W. Fong, C.Y. Chen, et al., IEEE Trans. Magn. 35 (1999) 910.

- [35] B.K. Yen, J.U. Thiele, M. Geissler, et al., *IEEE Trans. Magn.* 37 (2001) 1786.
- [36] T.W. Scharf, T.W. Wu, B.K. Yen, B. Marchon, J.A. Barnard, *IEEE Trans. Magn.* 37 (2001) 1792.
- [37] D.J. Li, Y.W. Chung, *IEEE Trans. Magn.* 39 (2003) 765.
- [38] D.J. Li, M.U. Guruz, C.S. Bathia, Y.W. Chung, *Appl. Phys. Lett.* 81 (2002) 1113.
- [39] P.H. Kasai, W.T. Tang, P. Wheeler, *Appl. Surf. Sci.* 51 (1991) 201.
- [40] B.D. Strom, D.B. Bogy, R.G. Walmsley, J. Brandt, C.S. Bhatia, *Wear* 168 (1993) 31.
- [41] S.C. Perry, C.M. Mate, R.L. White, G.A. Somorjai, *IEEE Trans. Magn.* 32 (1996) 115.
- [42] B. Tomcik, S.C. Seng, B. Balakrisnan, J.Y. Lee, *Diamond Relat. Mater.* 11 (2002) 1409.
- [43] P. Bernhard, C. Ziethen, R. Ohr, H. Hilgers, G. Schonhense, *Surf. Coat. Technol.*, in press.
- [44] C.Y. Chen, W. Fong, D.B. Bogy, C.S. Bathia, *Tribol. Lett.* 8 (2000) 25.
- [45] S. Anders, I. Brown, D. Bogy, C.S. Bathia, *Data Storage (October 1997)* 31.
- [46] H. Han, F. Ryan, M. McClure, *Surf. Coat. Technol.* 120–121 (1999) 579.
- [47] C. Casiraghi, A.C. Ferrari, R. Ohr, A.J. Flewitt, D.P. Chu, J. Robertson, *Phys. Rev. Lett.* 91 (2003) 226104.
- [48] M.G. Beghi, A.C. Ferrari, K.B.K. Teo, et al., *Appl. Phys. Lett.* 81 (2002) 3804.
- [49] K.B.K. Teo, S.E. Rodil, J.H. Tsai, A.C. Ferrari, S.E. Rodil, W.I. Milne, *J. Appl. Phys.* 89 (2001) 3707.
- [50] T. Witke, P. Siemroth, *IEEE Trans. Plasma. Sci.* 27 (1999) 1039.
- [51] D. Schneider, P. Siemroth, T. Schulke, et al., *Surf. Coat. Technol.* 153 (2002) 252.
- [52] B. Jacoby, A. Wienss, R. Ohr, M.V. Gradowski, H. Hilgers, *Surf. Coat. Technol.* (2003) 174–175.
- [53] R. Ohr, C. Shug, M. Wahl, et al., *Anal. Bioanal. Chem.* 375 (2003) 43.
- [54] C. Casiraghi, A.C. Ferrari, D.P. Chu, J. Robertson, *Diamond Relat. Mater.*, in press.
- [55] A. Wienss, G. Persch-Schuy, R. Hartmann, P. Joeris, U. Hartmann, *J. Vac. Sci. Technol. A* 18 (2003) 2023.
- [56] A. Wienss, G. Persch-Schuy, R. Hartmann, P. Joeris, U. Hartmann, *Appl. Phys. Lett.* 75 (1999) 1077.
- [57] C. Mathew Mate, B.K. Yen, D.C. Miller, M.F. Toney, M. Scarpulla, J.E. Frommer, *IEEE Trans. Magn.* 36 (2000) 110.
- [58] T.W. Scharf, J.A. Barnard, *J. Inf. Storage. Proc. Syst.* 2 (2000) 185.
- [59] H. Kohira, F.E. Talke, *Trans. ASME* 122 (2000) 288.
- [60] B.K. Gupta, A.K. Menon, *IEEE Trans. Magn.* 35 (1999) 764.
- [61] S. Sundararajan, B. Bhushan, *Wear* 225 (1999) 678.
- [62] E.V. Anokin, M.M. Yang, J.L. Chao, J.R. Elings, D.W. Brown, *J. Vac. Sci. Technol. A* 16 (1998) 1741.
- [63] S.S. Varanasi, J.L. Lauer, F.E. Talke, G. Wang, J.H. Judy, *J. Tribol.* 119 (1997) 471.
- [64] R.L. White, E. Schreck, R.H. Wang, *IEEE Trans. Magn.* 32 (1996) 110.
- [65] M.V. Gradowski, A.C. Ferrari, R. Ohr, et al., *Surf. Coat. Technol.* 174–175 (2003) 246.
- [66] A.-L. Barabasi, H.E. Stanley, *Fractal Concepts in Surface Growth*, Cambridge University Press, New York, 1995.
- [67] F. Family, *J. Phys. A* 18 (1985) L75.
- [68] X. Shi, L. Cheah, J.R. Shi, S. Zun, B.K. Tay, *J. Phys.: Condens. Matter* 11 (1999) 185.
- [69] P.I. Tamborenea, S. Das Sarma, *Phys. Rev. E* 48 (1993) 2575.
- [70] A. Libassi, B.K. Tanner, A.C. Ferrari, in: S.R.P. Silva (Ed.), *Properties of Amorphous Carbon*, EMIS Datareview Series No. 29, INSPEC, 2003.
- [71] B. Lengeler, in: M. Campagna, K. Rosei (Eds.), *X-ray Absorption and Reflection in the Hard X-ray Range*, North Holland, 1990.
- [72] L.G. Parrat, *Phys. Rev.* 95 (1954) 359.
- [73] B.K. Tanner, A. Libassi, A.C. Ferrari, J. Robertson, *Mater. Res. Soc. Symp. Proc.* 675 (2001) W11.4.
- [74] R. Ohr, B. Jacoby, M.V. Gradowski, C. Schug, H. Hilgers, *Surf. Coat. Technol.* 173 (2003) 111.
- [75] C.S. Bathia, C.Y. Chen, W. Fong, D.B. Bogy, *Mat. Res. Soc. Symp. Proc.* 593 (2000) 397.
- [76] R.J. Waltman, H. Zhang, A. Khurshudov, et al., *Tribol. Lett.* 12 (2002) 51.
- [77] J. Windeln, C. Bram, H.L. Eckes, et al., *Appl. Surf. Sci.* 179 (2001) 167.
- [78] W.C. Oliver, G.M. Pharr, *J. Mater. Res.* 7 (1992) 1564.
- [79] G.M. Pharr, D.L. Callahan, S.D. McAdams, et al., *Appl. Phys. Lett.* 68 (1996) 779.
- [80] T.A. Friedman, J.P. Sullivan, J.A. Knapp, et al., *Appl. Phys. Lett.* 71 (1997) 3820.
- [81] S. Xu, D. Flynn, B.K. Tay, et al., *Phil. Mag. B* 76 (1997) 351.
- [82] F. Nizzoli, J.R. Sandercock, in: G. Horton, A. Maradudin (Eds.), *Dynamical Properties of Solids*, North-Holland, Amsterdam, 1990, p. 281.
- [83] M.G. Beghi, C.E. Bottani, A.C. Ferrari, in: S.R.P. Silva (Ed.), *Properties of Amorphous Carbon*, EMIS Datareview Series No. 29, INSPEC, 2003.
- [84] D. Schneider, Th. Witke, Th. Schwarz, B. Schneich, B. Schultrich, *Surf. Coat. Technol.* 126 (136) (2000) 136.
- [85] M.G. Beghi, C.E. Bottani, D. Schneider, et al., *C4/F2-8, ICMCTF 2003*, San Diego.
- [86] A.C. Ferrari, J. Robertson, *Phys. Rev. B* 61 (2000) 14095.
- [87] F. Tuinstra, J.L. Koenig, *J. Chem. Phys.* 53 (1970) 1126.
- [88] A.C. Ferrari, J. Robertson, *Phys. Rev. B* 64 (2000) 75414.
- [89] K.W.K. Gilkes, H.S. Sands, D.N. Batchelder, J. Robertson, W.I. Milne, *Appl. Phys. Lett.* 70 (1997) 1980.
- [90] J. Koskinen, J.P. Hirvonen, J. Keranen, *J. Appl. Phys.* 84 (1998) 648.